Tiltrotor airframe flow field characterization by SPIV.

CONFERENCE PAPER · SEPTEMBER 2015

READS
7

3 AUTHORS:

Fabrizio De Gregorio
CIRA Centro Italiano Ricerche Aerospaziali
70 PUBLICATIONS **171** CITATIONS
SEE PROFILE

Giovanni Fatigati
CIRA Centro Italiano Ricerche Aerospaziali
1 PUBLICATION **0** CITATIONS
SEE PROFILE

Stephan Kallweit
Fachhochschule Aachen
20 PUBLICATIONS **35** CITATIONS
SEE PROFILE

11TH INTERNATIONAL SYMPOSIUM ON PARTICLE IMAGE VELOCIMETRY – PIV15
Santa Barbara, California, September 14-16, 2015

Tiltrotor airframe flow field characterization by SPIV.

Fabrizio De Gregorio[1], Giovanni Fatigati[1] and Stephan Kallweit[2]

[1] Experimental aerodynamics group, Italian Aerospace Research Centre, Capua, Italy
f.degregorio@cira.it

[2] Intelligent Laser Applications GmbH, Jülich, Germany

ABSTRACT

To achieve consistent Drag reduction of airframe and nonlifting rotating systems of the Green Rotorcraft ITD, the EU launched the JTI CleanSky GRC2 project. In its framework, a CFD-based optimization activity has been carried out along with experimental tests on the ERICA tiltrotor configuration in order to analyse the effect on flow field and drag of the optimised geometries. In this paper, a characterization of the ERICA tiltrotor aft fuselage wake is given based on an experimental wind tunnel test campaign. The wind tunnel tests were carried out on the unpowered 1:8 scale ERICA model in the RUAG LWTE wind tunnel aiming to characterize the aft fuselage wake via stereo PIV measurements for both the baseline and optimised sponsons. The observed flow structures are analysed and linked to the drag reduction obtained with the optimized sponsons in comparison with the baseline sponsons.
The ensemble average flow field results are discussed in terms of wake macrostructures, velocity magnitude, momentum loss, vortex flow and vortex characteristics in relation to the model attitude and configuration. The flow field shows well the rise and the development of the aft fuselage wake as well as a net difference between the baseline configuration and the optimised one. The comparison of the Momentum and of the Momentum loss between the configurations is discussed together with the vortex flow characteristics. The wake behaviour in terms of peak vorticity is discussed also in terms of instantaneous velocity fields in comparison with POD-based low-order-reconstructed velocity field for different numbers of modes and with the mean velocity.

1 INTRODUCTION

The peculiar characteristic of the tilt-rotor is the capability to take-off and land like a helicopter and at the same time to cruise like an airplane. This is achieved by tilting the rotor nacelles perpendicular to the flight direction, in helicopter mode, or parallel to the flight direction, in aircraft mode. The most recent tiltrotor concepts (such as the European civil tiltrotor ERICA [1]) share some advantageous features of the traditional tiltrotors with the tilt-wing aircraft, i.e. the capability of tilting the outboard portions of the wings independently from the proprotor. This configuration removes the loss of thrust due to the downwash of the rotors on the wings in helicopter mode, giving the opportunity to reduce the rotor dimensions and thus improve cruise performance. Moreover, the smaller dimensions of the rotors gives the tiltrotors like ERICA STOL (Short Take-Off and Landing) capabilities, meaning that take-off and landing in airplane mode are possible. An aerodynamic optimization in terms of drag increases flight speed, operational range, load capability, reduces the fuel consumption and consequently the environmental impact and enhances the economic appeal of the new concept. While tiltrotors operate under a wide range of flight conditions, from hover to cruise passing through several intermediate states, the primary focus for aircraft performance optimisation lies on the cruise phase. In cruise, tiltrotors can be likened to conventional transport aircrafts, specifically to regional turboprop aircrafts. The typical drag breakdown of a generic transport aircraft [2] is illustrated on the left of Figure 1. Viscous and lift induced drag contribute by approximately 85% to the total value. The next largest contribution, 10% of the overall drag, is due to the afterbody wake shedding and the resulting pressure drag. The remaining contributions come from aerodynamic interference phenomena, roughness, leakage and shock wave drag. This last contribution can be neglected for the tiltrotors due to the low cruise speed. In the recent past, in order to evaluate the drag build-up of the ERICA airframe and its rotating non-lifting components, a wind tunnel test campaign was carried out with a non-motorised scaled model [3]. The result (Figure 1 right) shows that the fuselage, the wing/fuselage fairings, the sponsons, the fin and tail plane represent about 50% of the total measured body-induced drag. Therefore, a considerable reduction in power requirement is expected to be achievable by increasing the aerodynamic efficiency of the tiltrotor airframe and the rotating non-lifting components.

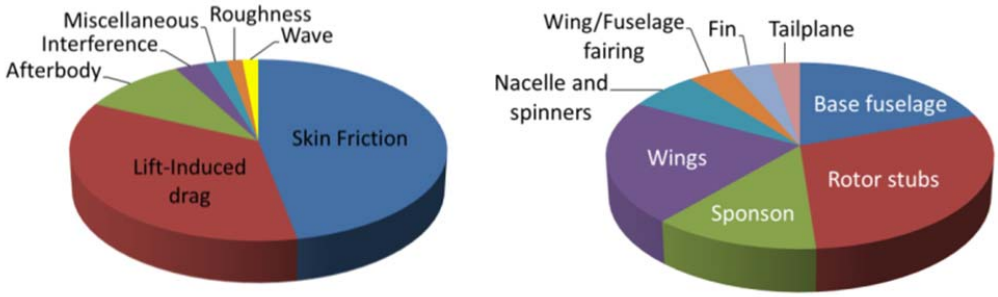

Figure 1: Transport aircraft Drag Breakdown (left) and ERICA Body induced drag Breakdown (right)

In the framework of the CleanSky sub-project GRC2 "Drag reduction of airframe and non-lifting rotating systems" of the Green Rotorcraft ITD, a CFD-based optimization activity has been carried out, resulting in optimised shapes of the tiltrotor fuselage **Errore. L'origine riferimento non è stata trovata.**. The assessment of the new optimised geometry, obtained coupling CFD with an innovative design methodology based on evolutionary algorithms [5], was carried out in the framework of the DREAm-TILT project [6]. The aerodynamic performance of the ERICA baseline was compared to the optimised components and the singular and global benefit in terms of efficiency and in particular drag reduction were evaluated. Together with the aerodynamic load measurements, the test campaign foresaw the flow field characterization by means of Stereo Particle Image Velocimetry (S-PIV) of the fuselage wake downstream the landing gear sponsons. The tests were executed in RUAG LWTE wind tunnel (Figure 2). Being the time occupancy of such types of industrial facilities relatively expensive, a high test productivity and therefore a low measurement time are mandatory. Typically the CFD validation is carried out by comparing the predicted and the measured mean global forces. Similarly the CFD flow field assessment is performed by comparing the predict flow field statistics with the S-PIV mean velocity field although the wake shedding is a highly unsteady phenomenon. In order to obtain accurate mean velocity fields and to limit the wind tunnel occupancy, the number of instantaneous velocity fields for each test case was about 150 images [7].

Figure 2: ERICA model in RUAG LWTE Test Section – Front View

These wake flow measurements were carried out to better understand the flow mechanisms responsible for the benefits observed for the new optimised sponsons. The evaluation of the aerodynamic benefit of the optimised sponsons compared with the baseline configuration and in particular the wake behaviour is the main goal of this work. The flow field measurements are analysed in terms of mean velocity fields for the different model attitudes and configurations. The momentum and momentum loss are calculated and related to the percentage drag reduction obtained by the optimised model in comparison with the baseline. The main flow structures and in particular the counter rotating vortices, arising on the sponsons and drawn downstream by the flow itself, are investigated comparing the vorticity peaks behaviour for the different configurations. Furthermore, being the wake shedding downstream the landing gear sponson an unsteady phenomenon characterised by two main counter rotating vortices, the instantaneous vorticity fields have been investigated in comparison with the mean values. A proper orthogonal decomposition (POD) based low order reconstructed (LOR) velocity fields has been adopted in order to remove the outlier vectors from the instantaneous velocity fields as suggested by Gunes and Rist [15] and by Wang et al [16]. The benefit obtained respect to the mean and instantaneous velocity are hereafter discussed.

2 EXPERIMENTAL SET-UP

2.1 Test Facility and Model Description

The test campaign was carried out in the RUAG LWTE wind tunnel. The LWTE is an atmospheric closed loop wind tunnel with a 7x5 m^2 (WxH) cross section. The mock-up used during the tests was a 1:8 scaled model of the ERICA tiltrotor on which the original geometries have been replaced with optimized ones (nose and wing/fuselage fairing) studied during previous tests. The model was unpowered and the rotor blades were replaced by fixed stubs. The model's main dimensions were: wing span b_w=1.875 m, mean aerodynamic chord mac=0.3038 m, fuselage length L= 2.1 m and wing surface S_w= 0.578 m^2. The modular model build-up allowed to investigate the singular influence of the different optimized components on the aerodynamic loads. For the flow field measurements, the model was mounted in the up-right position supported by the tunnel pylon. Both the sets of sponsons, baseline and optimised, were used (see Figure 3). In order to have a clean bottom model and minimize the disturbances in the regions of interest (sponsons), the dorsal configuration was used to mount the strut. Because of the mounting position, that caused the empennage to be in the wake of the tunnel pylon, it was chosen to remove the empennage so as to have cleaner balance measures. The tests were carried out at a constant wind speed of V_∞=50 m/s, corresponding to a Reynolds number based on the mean aerodynamic chord of approximately Re=930.000.

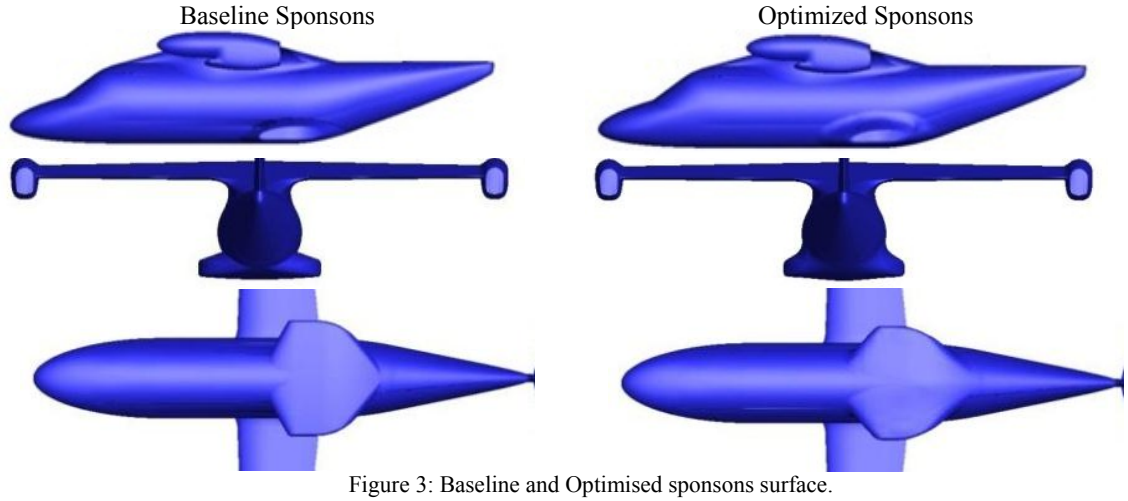

Figure 3: Baseline and Optimised sponsons surface.

2.2 Instrumentation and Data Acquisition

The aerodynamic forces and moments acting on the wind tunnel model were acquired via an internal six component balance (RUAG 192). The static accuracy of the balance is in the order of 0.1 % of the design loads for all components and load combinations over the entire measurement range. Secondary instrumentation included, amongst other sensors, Schaevitz LSRP inclinometers with an accuracy of 0.03° for recording the actual pitch and roll attitude of the model. Different corrections have been applied to the wind tunnel data. The effects of blockage and flow angularity have been corrected using a wall pressure signature method [8].

2.3 Flow field measurements

The Stereo PIV measurements were carried out on four different vertical cross planes at different distances from the model nose (x/L=0.74, 0.79, 0.83, and 0.93) and respectively named as PIV1, PIV2, PIV3 and PIV4. An additional plane PIV5 at x/L=0.88 was measured only for the baseline configuration. The measurement planes for both model configurations are shown in Figure 4. The measurement planes were not symmetric respect the model centreline but centred slightly on the left of the model.

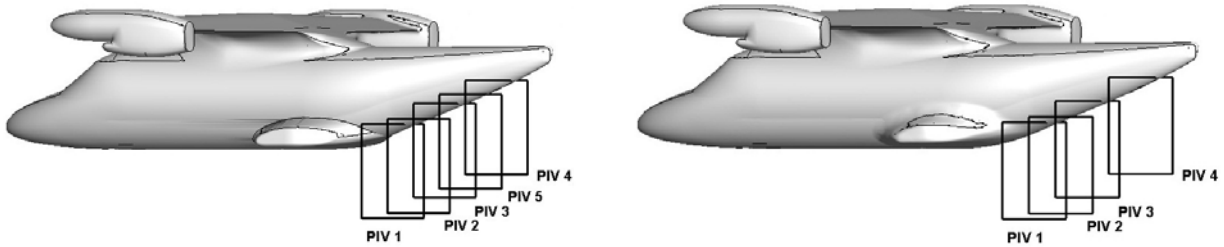

Figure 4: PIV recording region: Baseline Sponsons (left) and Optimized Sponsons (right)

The adopted measurement system was related to the wind tunnel reference system and no rotations occurred when the model incidence angle varied. The reference system foresees: the x-axis oriented as the free-stream velocity and laying on the model symmetry plane, the z-axis along the vertical and upward oriented, the y-axis is oriented following the rule of the right hand. The origin was located at 150mm upstream the model nose and 209.87mm below the model nose for null model incidence angle as shown in Figure 5.

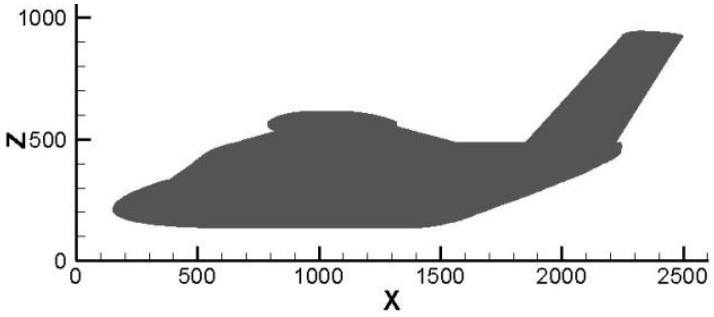

Figure 5: Adopted reference system

The PIV system was composed of two Nd-Yag resonator heads providing a laser beam of about 250 mJ each at 532 nm and by two double frame CCD cameras (2048x2048 px). Particles of about 1 μm of diameter of DEHS oil, were used as seeding. The seeding was injected downstream of the test section in order to obtain uniform seeding concentration of the full circuit. The laser was locatedbeneath the test section. The laser light sheet was projected upward into the test section through an acrylic window installed in the test section floor. The light sheet optics were mounted on a linear traversing system remotely controlled in order to translate it along the wind tunnel longitudinal axis. Each recording camera was mounted on a 2D linear traversing system and located outside of the test section downstream the model. The optical access was through the frames of the side wall rear doors, downstream of the model. The traversing systems allowed to rigidly move the cameras and light sheet plane without the need for additional calibrations of the stereo set up, increasing significantly the measurement productivity. Each camera was equipped with a motorised Scheimpflug support, 200 mm Canon EOS lens and lens remote control. The viewing angle between the stereo cameras was of about 96° close to the optimum values of 90°. The stereo lay-out is illustrated in Figure 6.

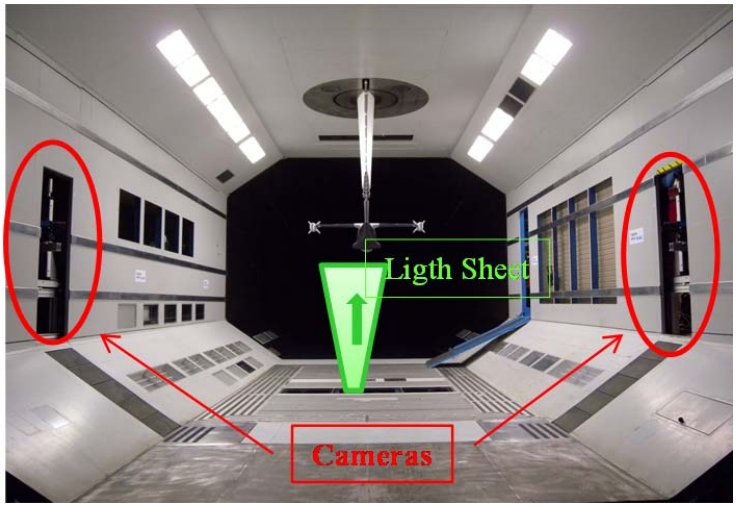

Figure 6: Recording lay-out in RUAG LWTE TS

The stereo PIV cameras recorded a field of view of 500x346 mm^2 providing a velocity vector spatial resolution of about 4.5 mm/vector on both directions. The test matrix foresaw testing with two model configurations, model incidence angles (α) varying from -6° to +2° with steps of 2° and one additional point at +10°, yaw angles (β) ranging from -5° to +5° with steps of 5° and S-PIV measurements on five parallel planes for a total number of 66 test cases.

3 PIV DATA POST-PROCESSING

PIV image post processing has become a standard procedure that retrieve many flow statistics from the analysis of the PIV images then further analyses can be applied to the results to achieve a better understanding of the aerodynamic phenomena observed.

3.1 Pre-processing

The images pre-processing procedure has been tuned in order to properly compare the results taking into account that the momentum calculation is fairly sensitive to the integration size and to the body reflections. It is worth to underline that the sets of images obtained for the two cases differ only by the vertical position of the cameras. As first step the maximum image from the PIV set of data of each configuration was evaluated so as to embed in it all the hot pixels. This allowed to mark the body reflections and camera blooming regions. Once the masks were detected for optimised and baseline configuration, the mask providing the complete removal of spurious vector in proximity of the model was selected for both configurations. In this way, the same area of integrations was assured. The pre-processed images were analysed by a multi-grid algorithm [10], using a pyramidal approach by starting off with larger interrogation windows on a coarse grid and refining the windows and grid with each pass. Starting from the instantaneous plane velocity components (v and w) the out of plane component of the vorticity was calculated ω_x. Furthermore the following statistical quantities were evaluated: the ensemble average velocity field, the standard deviation of the velocity components, and the Reynolds stresses components: u'u',v'v', w'w', v'w', v'u', w'u'.

3.2 Accuracy Estimation

An estimation of the measurement accuracy was performed. Following the work of Adrian [11], the number of pixels/particle for the adopted experimental set up was determined. First the image diameter d_s of the focal spot produced by a zero diameter particle was calculated, given by the following formula:

$$d_s = 2.44*(1+M)*f\#*\lambda \tag{1}$$

where f# is the lens f-number, *M* is the image magnification factor, and λ is the wave number of laser light. Using this result along with particle diameter d_p, magnification factor M and CCD pixel resolution (d_r=7.4 μm), the image diameter of the particle on the CCD sensor d_e was obtained by:

$$d_e = \sqrt{M^2 d_p^2 + d_s^2 + d_r^2} \tag{2}$$

where d_p was the actual particle diameter (1μm). Carrying out the calculations using the data summarised in Table 1 it was found a value of 1.40 pixels per particle. The pixel particle ratio being larger than 1 assured minor effect due to the pixel locking effect.

f#	d_r (10^{-6} m)	d_p (10^{-6} m)	d_s (10^{-6} m)	d_e (10^{-6} m)	pixel/particle
4.7	7.4	1	7.27	10.38	1.40

Table 1: Calculation of the pixel particle ratio

The PIV data uncertainty was evaluated according to the standard procedures given by Raffel et al [12]. The random noise of the displacement was considered smaller than 0.05px. Minor bias errors were expected, including minor effects of peak-locking being the value of the pixels per particle larger than 1 (d_e/d_r=1.4). However, based on the displacement histograms, the bias error was estimated to fall below random noise, i.e. less than 0.05px. The resulting velocity error ε_u was estimated as:

$$\varepsilon_v = \varepsilon_y / (\Delta t\, M) \tag{3}$$

where Δt is the pulse-separation time and M is the optical magnification. Scaling with the maximum in-plane velocity component V_{max} the relative error $\varepsilon_{v,\,rel} = \varepsilon_v / V_{max}$ was determined as

$$\varepsilon_{u,\,rel} < U_{max} / V_{max} \cdot 3/(\Delta X \cdot M) \cdot \varepsilon_y \tag{4}$$

where, U_{max} is the maximum out-of-plane component of the flow velocity, ΔX is the light-sheet thickness, and ε_y is the displacement uncertainty in pixel dimensions. Due to the recording geometry and the measurement uncertainty, the out-of-plane measurement error ε_u was approximately a factor of √2 higher than that of the in-plane measurement. The error estimation for some indicative test cases, for the displacement error of $\boldsymbol{\varepsilon_y}$ = 0.05px are summarized in Table 2.

Configuration	Pitch angle [°]	x/L [-]	M [10^3 px/mm]	Dz [10^{-3} m]	U_{max} [m/s]	W_{max} [m/s]	ε_x [px]	ε_u [m/s]	ε_w [m/s]	ε_{urel} [%]	Δt [10^{-6} s]
Baseline	10	0.74	5.2	5	29.6	58.8	0.05	1.92	2.72	1.15	5
Baseline	10	0.79	5.2	5	43.0	64.5	0.05	1.92	2.72	0.87	5
Baseline	2	0.93	5.2	5	24.5	54.0	0.05	1.92	2.72	1.27	5
Optimised	2	0.93	5.2	5	22.1	52.0	0.05	1.92	2.72	1.36	5

Table 2: Summary of main PIV recording data, processing settings and error estimation.

3.3 Momentum and Momentum loss calculation

A well-known experimental technique in wind tunnels to estimate the drag of a wing is the wake-survey method. It consists in calculating the aerodynamic loads acting on a body from an integration of the flow variables inside a control volume surrounding this object [9]. Proper control volume boundaries such as upper, lower and lateral surfaces corresponding to streamlines, front and rear surfaces corresponding to planes perpendicular to the freestream velocity and located far upstream and downstream of the model and the steady state condition for the flow field simply the equation. When applied only to the drag evaluation it reduces to the momentum deficit in the wake ([13],[14])

$$D = \iint_S \rho U(V_\infty - U)dS \tag{5}$$

For the present test, the data available are instead measured in the vicinity of the body. The full equation for the momentum conservation should be applied, having only the unsteady term cancelled out:

$$D = \iint_S \rho U(V_\infty - U) + (p_\infty - p) - \vec{n} \cdot \bar{\bar{\tau}} \cdot \vec{n}dS \tag{6}$$

It is understood that the contribution of pressure and stresses becomes negligible moving downstream and approaching the conditions of equation (5). These two terms are not measured in the present work therefore the analysis of the wake evolution and the drag estimation are performed using only the momentum. The x-component of the Momentum (M_X) and the Momentum loss (ΔM_X) are therefore given respectively by the following equations:

$$M_X = \iint_A \rho U^2 dA \tag{7}$$

$$\Delta M_X = \iint_A \rho U(V_\infty - U)dA \tag{8}$$

where ρ is the air density, U is the X component of the velocity at the measurement section, V_∞ is the X component of the velocity at the upstream inlet section, A is the surface of the front and rear crosswise boundaries.

The equations (7) and (8) were applied to PIV mean velocity by reducing the integration domain to a sub-region covering the released wake. For the low subsonic condition, the incompressibility assumption was adopted and the air density was set equal to 1.225 $\frac{kg}{m^3}$.

As the result of the integrations is highly affected by the extent of the domain of integration, the area on which the integration of the Momentum and the loss of Momentum was calculated was exactly the same in order to allow a correct comparison between baseline and optimised sponsons.

3.4 Proper Orthogonal Decomposition

POD is an approach for data analysis aiming to approximately describe a high/infinite-dimensional dynamical problem using a low-dimensional model. It was first applied to study turbulent flows by Lumley [17] and reviewed by Berkooz et al. [18]. The idea of POD is to extract prominent modes associated with high-energy containing large-scale coherent structures in turbulent flows, thereby achieving a mode reduction from a full dimensional turbulence to a low-dimensional model.

Hereinafter a brief remainder is given of the working principle of the POD method; for details, the reader is referred to Sirovich [19]. The POD approach provides an energy efficient decomposition of the fluctuating part of a velocity field:

$$\vec{u}(\vec{x},t) = \vec{U}(\vec{x}) + \vec{u}'(\vec{x},t) = \vec{U}(\vec{x}) + \sum_{n=1}^{N} a_n(t)\overrightarrow{\Phi_n}(\vec{x}) \quad \textbf{(9)}$$

where U and u' denote the mean and fluctuating components of the velocity field. The normalized base functions $\overrightarrow{\Phi_n}$ are spatially orthogonal, while the mode coefficients a_n are uncorrelated in time:

$$< \overrightarrow{\Phi_i} \cdot \overrightarrow{\Phi_j} > \begin{cases} 1, (i=j) \ \overline{a_i a_j} = \lambda_i \\ 0 \ (i \neq j) \end{cases} \quad \textbf{(10)}$$

The angled brackets and overbar indicate spatial integration and temporal averaging, respectively. The POD modes $\overrightarrow{\Phi_n}$ are obtained as the eigen modes of the two point correlation matrix:

$$\boldsymbol{C}\overrightarrow{\Phi_n} =; \ with \ C_{ij} = \overline{\vec{u}'(\overrightarrow{x_i},t) \cdot \vec{u}'(\overrightarrow{x_j},t)} \quad \textbf{(11)}$$

The eigenvalue λ_n represents the contribution of the corresponding POD mode to the total fluctuating energy:

$$< \overline{\vec{u}'(\overrightarrow{x_i},t) \cdot \vec{u}'(\overrightarrow{x_i},t)} >= \sum_{n=1}^{N} \lambda_n \quad \textbf{(12)}$$

Sorting the POD modes in order of decreasing eigenvalues reveals the most dominant (i.e., energy containing) modes. In a flow field, outliers physically act as strong fluctuations. Since POD is highly associated with velocity fluctuations and turbulent kinetic energy, has been verified that outliers increases the total turbulent kinetic energy and contribute the energy to the higher modes [16]. POD analysis is a powerful post-processing tool to identify dominant coherent flow patterns and to construct reduced-order flow models that capture the largest amount of energy with the smallest number of modes and at the same time remove the outliers.

4 RESULTS

The experimental assessment of the fuselage geometry optimization in terms of drag reduction was the main scope of the DREAm-TILT project. Even though during the flow field measurements the model had no empennage, the aerodynamic loads were recorded so as to be able to compare the flow field measurements with those coming from the balances. Hereafter both the balances and the PIV results are shown.

4.1 Aerodynamic loads measurements

The comparison of the aerodynamic loads for the optimised sponsons versus the baseline sponsons for a sweep polar in the range between α=-5° and α=+5° shows a fairly identical behaviour of the lift coefficient except for an nearly negligible reduction of the lift slope (Figure 7 top left) and a clear benefit in terms of drag reduction in the range between 15 to 30 drag counts (0.0001 of drag coefficient, Figure 7 top right). Due to the lack of the empennage, the pitching moment shows an unstable behaviour (Figure 7 bottom left), the model with the optimised sponsons reveals even strongly this attitude. The efficiency of the optimised configuration is thus clearly improved: at the same lift coefficient the drag is reduced (Figure **7** bottom right).

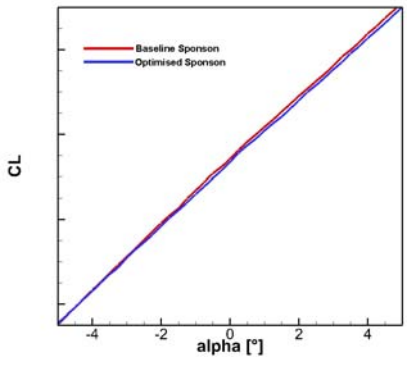

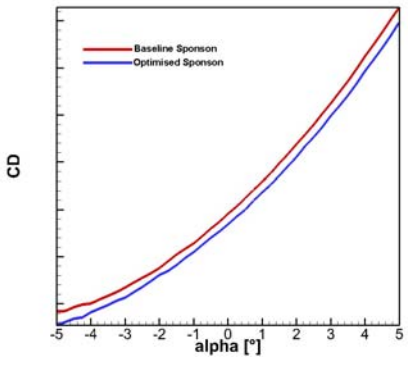

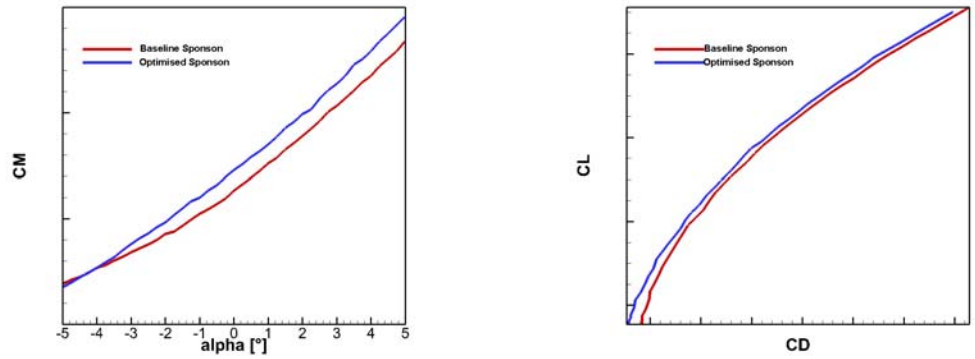

Figure 7: Optimised/Baseline sponsons configuration comparison. CL (top left), CD (top right) and CM (bottom left) vs α. CL vs CD (bottom right)

The baseline configuration presented a clear increase of the drag coefficient for the sweep polar with yaw angle of β=-5° in comparison with β =0° (Figure 8 left). The CD increment for β=-5° is in the range between 3.2% to 6.7%, depending on the incidence angle. Similarly the pitching moment coefficient shows a growth for β =-5°, with a further increase of the unstable behavior (Figure 8 centre). The efficiency for β=-5° is reduced, at the same lift coefficient the drag is increased (Figure 8 right). The optimized configuration presented similar behavior, but the drag increase was limited in the range between 2.9% to 5.4%, indicating a better efficiency with respect to the baseline.

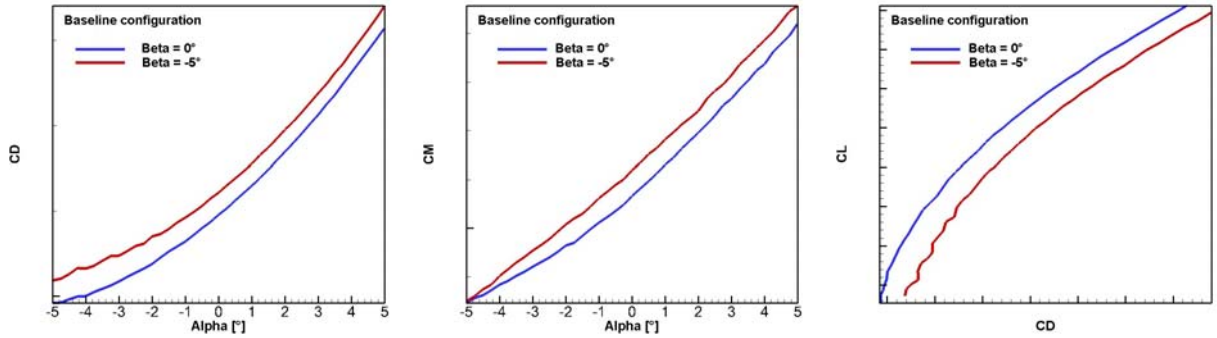

Figure 8: Baseline varying the yaw angle. CL vs a (left), CM vs a (centre) and CL vs CD (right)

4.2 Flow Field measurements

The flow field measurements were aimed to investigate and compare the flow characteristics of the wake behind the ERICA baseline sponsons and the new optimised geometry. The region of interest was located underneath the Tiltrotor fuselage and downstream of the sponsons. This region typically is responsible for the aft body drag component induced by flow separation and counter rotating vortex shedding. The flow field was investigated at various incidence and yaw angles.

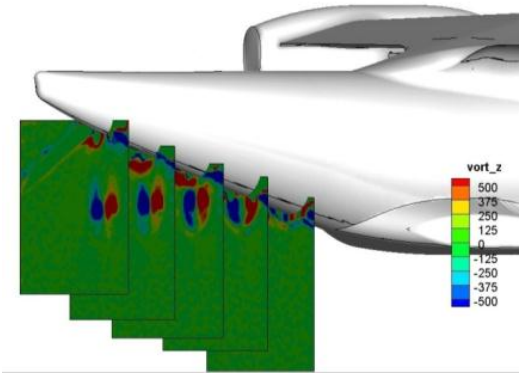

Figure 9: Out of plane vorticity field

The pitch ranged between α=+2° to α=- 4° with angular steps of 2° and a few cases for α =+10° and -6° whereas the yaw was mostly set to β=0° and at β=-5° and only one at β=+5° for symmetry check. Each condition was investigated for both model configurations, with only few exceptions. The plane located at x/L=0.88 was measured only for the baseline case due to wind tunnel time constraints. An example of the wake measurement in relation to the model geometry is shown in Figure **9** as colour map of the out-of-plane vorticity. The shown case presents the baseline configuration at α=+2° and β=0°.

4.2.1 Velocity Magnitude

The velocity magnitude colour map together with the in-plane velocity vectors clearly displays the flow macro structures arising on the fuselage, growing in the proximity of the fuselage and eventually detaching from it (Figure 10). The results are presented as a comparison between the velocity magnitude colour plots measured on the baseline sponson model configuration (upper row in Figure 10) and the improved sponson configuration (lower row in Figure 10) at the different cross planes. The case characterised by α=+2° and β=0° shows for the baseline configuration and on the first measurement plane x/L=0.74, the development of a thin symmetric wake in the proximity of the fuselage bottom.

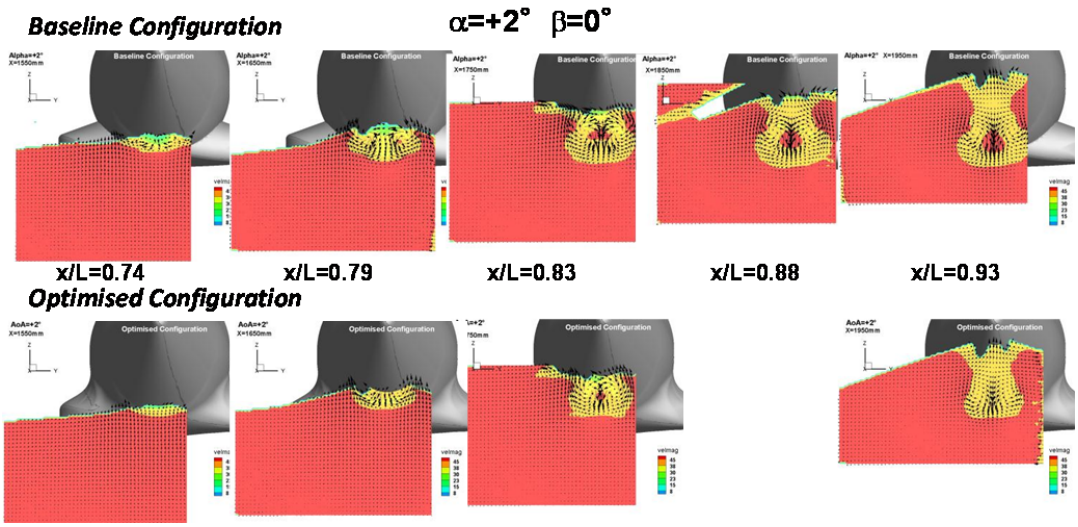

Figure 10: PIV Velocity vector field with velocity magnitude colour map at α=+2° and β=0°. Upper row baseline configuration results. Bottom row optimised sponson configuration results.

The wake then moves downstream along the fuselage, increasing in size until it detaches from the fuselage at x/L=0.83 and clearly shows the presence of the two counter rotating vortices. Moving further downstream, the vortices are observed to move downward and the fuselage wake stretched vertically. The flow field induced by the optimised sponsons presents a similar behaviour but is characterised by: a smaller wake size, reduced momentum loss, delayed separation and higher closeness of the vortices to the model.

4.2.2 Momentum analysis

In the Drag development process, due to the skin friction, each cross section of the body contributes to the drag growth. Thus moving from the nose of the aircraft to its tail this part of the drag raises up. The pressure distribution on the fuselage tail, which is the recovery pressure zone, gives another contribution to the drag also because of the presence of separated flow. Similarly to the skin friction contribution the pressure contribution makes the drag increase moving far away from the sponsons in the downstream direction. As described in § 3.3, the evolution of the drag along X-axis was studied by integrating the X component of the Momentum over several domains along the longitudinal axis.

The case at α=+2° and β=0° was analysed by investigating how the improvement in the flow field characteristics reflected on the variation along the X axis of the X-component of the Momentum (equation (7)). Considering that such variation is a part of the aft body drag and that the optimised configuration presented smaller drag coefficients it's not surprising that the total Momentum of the optimised configuration is higher than that evaluated for the baseline sponson configuration (diamond marks of Figure 11 left). Reversely the optimised Momentum loss (equation (8)) is smaller comparing with the baseline configuration (circle marks in Figure 11 left).

The diagram shows that moving from x/L=0.74 to 0.83 the Momentum decrease and the Momentum loss increase, complying with the fact that the wake under the fuselage enlarges as shown in Figure 10. This is coherent also with the drag increase while moving downstream. At x/L=0.83 a region with high speed appears between the two vortices. The air sucked and accelerated by the vortices from the boundary layer is expulsed partly in the out-of-plane direction.

Moving downstream, the vortices, being no longer energised by the boundary layer, dissipate as the viscosity and the shear layer makes them transfer the energy to the near flow regions. The Momentum remains nearly constant as well as the Momentum loss, they even seems to recover a bit.

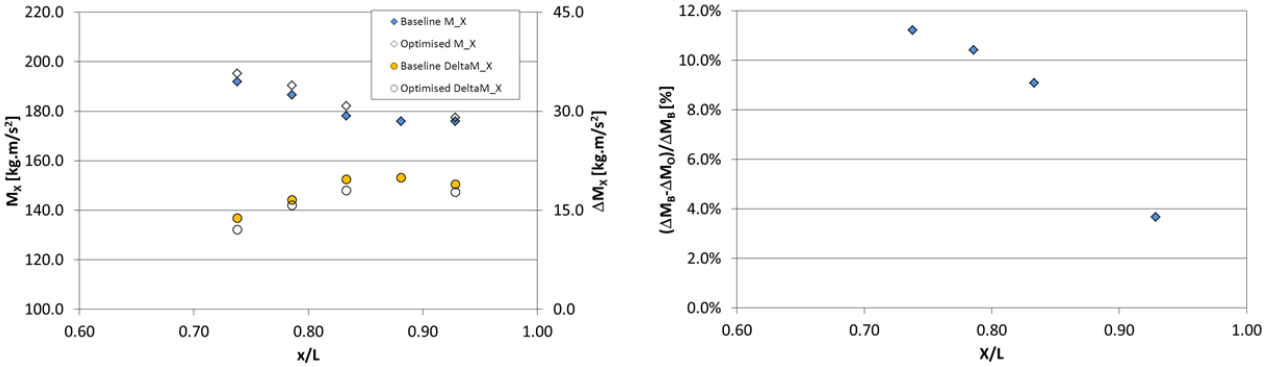

Figure 11: X-component of the Momentum and of the Momentum loss evaluated at the different PIV planes (left). Percentage variation of the X-component of the Momentum between the baseline and optimized configurations (right).

The percentage variation of the Momentum loss between the baseline configuration and the optimised one (Figure **11**-right) shows larger values (x/L=0.74) in proximity of the sponsons for later decrease moving further downstream. At x/L=0.74, the baseline configuration shows a wake growth thicker than those of the optimised one and the percentage variation is about 11.2%. Moving downstream this difference decreases even though the baseline configuration boundary layer remains thicker. Despite an outstanding difference between the flow fields of the two configurations at x/L=0.93, the percentage variation of the Momentum losses decreases to 3.7%. It is worth to underline that the percentage variation of the momentum loss is related to the percentage difference of the drag coefficient between the two configurations. For α=+2° and β=0° the measured drag percentage variation was equal to 2%, and the diagram indicates that the trend is going to approach this value moving further downstream the model.

4.2.3 Vortex development

Interesting conclusions can be drawn by analysing the out-of-plane vorticity of the ensemble average velocity fields. In Figure 12, for the same case discussed above (α=+2° and β=0°) the baseline model configuration at x/L=0.74 shows a weak trace of the presence of two counter rotating vortices. The vortices are clearly detectable in proximity of the fuselage at x/L=0.79 and fully developed at x/L=0.83 but still confined in the proximity of the fuselage. The real vortex detachment is evident at x/L=0.88 and moving further down at x/L=0.93.

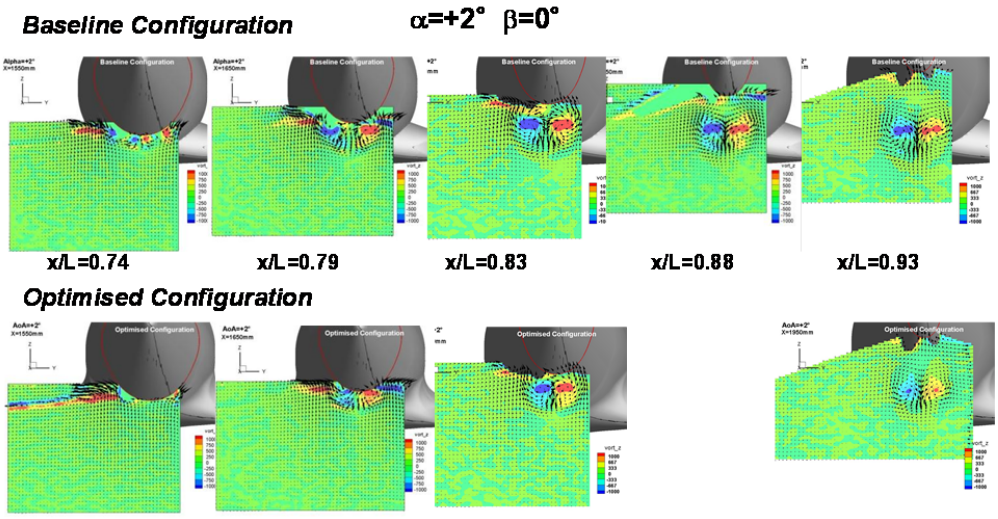

Figure 12: Out of plane vorticity colour map at α=+2° and β=0°. Upper row Baseline results and lower row Optimised ones

The vortex intensities increase from x/L=0.79 to 0.83 and later decrease when fully detached. The out of plane vorticity distribution (ω_x) measured along the axis connecting the vorticity peaks of the counter rotating vortices shows the

quantitative behaviour at different distances along the longitudinal axis (Figure **13** left). The vortex behaviour is explained by the fact that up to x/L=0.83 the vortices are still connected to the fuselage and energised by the flow around the fuselage. Once the vortices are fully separated, the dissipation starts spreading the energy to the adjacent zones. The related case for the optimised sponsons indicates at x/L=0.74 a fairly attached flow, the counter rotating vortices start to be visible underneath the fuselage at x/L=0.79 and are fully developed in the proximity of the fuselage at x/L=0.83. The vortices separate from the fuselage at x/L=0.93. The vortex development for the optimised configuration along the fuselage is similar to the baseline case: the vorticity increases during the vortex growth and later decreases as the vortices separate from the fuselage. The ω_x behaviour at different positions along the x-axis is shown in Figure 13 right.
The quantitative comparisons of the out of plane vorticity extracted along axis passing through the vorticity peaks of the contra rotating vortices for the baseline and the optimized configuration, are shown in Figure 14. The optimised case is characterised by smaller structures and the vortex intensity is reduce respectively of about 40%, 25% and 21% at x/L=0.79, 0.83 and 0.93 in comparison with the baseline configuration. The vortices also remain closer to the surface and could induce stronger tangential velocity and hence generate a lower pressure distribution resulting in a higher contribution to the drag.

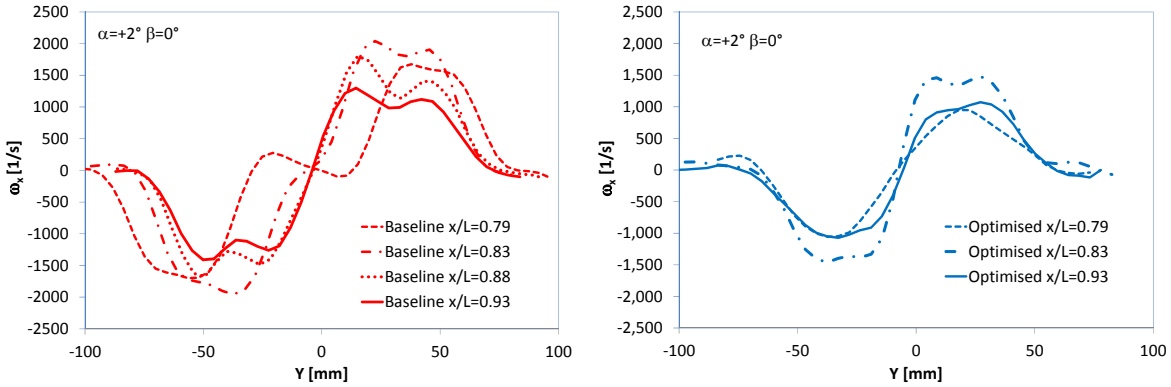

Figure 13: PIV peak vorticity comparison at different x/L for the baseline (left) and optimized configuration (right)

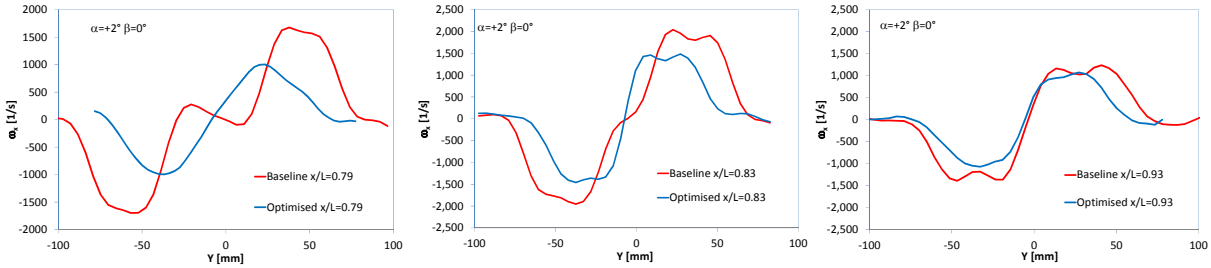

Figure 14: Baseline and Optimised ω_x comparison at: x/L=0.79 (left), x/L=0.83 (centre) x/L=0.93 (right)

The counter rotating vortices behavior is investigated at β=-5° for both configurations (Figure **15**). The baseline configuration shows the presence of a couple of vortices at x/L=0.79. Moving downstream the left vortex moves closer to the more intense right vortex (X/L=0.83) and at x/L=0.93 almost disappears overwhelmed by the right vortex. The ω_x distribution along the peak vorticity indicates for the baseline at x/L=0.79 almost the same value for the negative and positive peak, the absolute value is about ω_x=2100 s^{-1}, at x/L=0.83 the minimum peak decreases to ω_x=-1600 s^{-1} whereas the positive peak is energized to ω_x= 2350 s^{-1}, at x/L=0.93 the negative peak drops down to ω_x=-600s^{-1} while the positive peak decreases to ω_x =1800 s^{-1}, three times higher than the negative peak (continuous line in Figure 16). The optimized configuration presents a similar behavior but characterized by less intense vortices (Figure 15 bottom data). The intensity reduction can be estimated in about 35% of the intensity of the vorticity. At x/L=0.83 the vorticity distribution indicates similar values for the negative (ω_x=-1275 s^{-1}) and positive (ω_x=1150 s^{-1}) moving at x/L=0.93 the negative peak decreases to (ω_x=-390 s^{-1}) while the positive peak increases to (ω_x=1230 s^{-1}) also in this case the positive peak is three times higher than the negative (dashed lines in Figure 16).

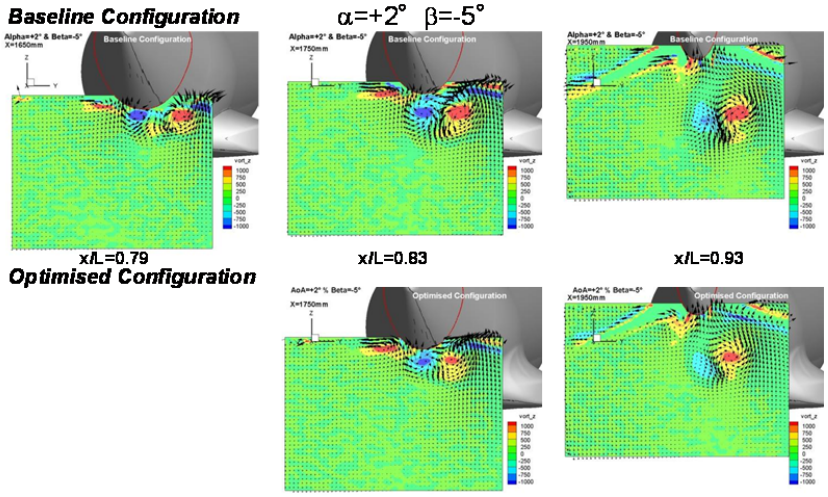

Figure 15: Out of plane vorticity colour map at α=+2° and β=-5°. Upper row Baseline results and lower row Optimised ones

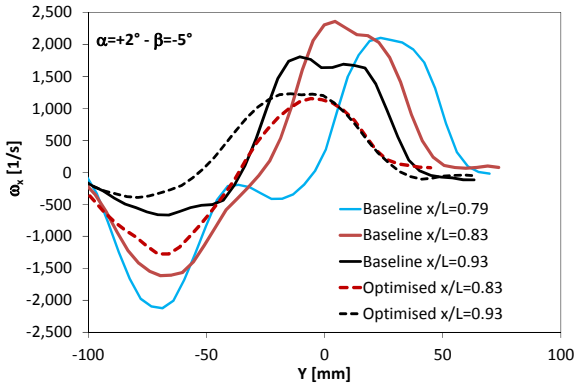

Figure 16: PIV peak vorticity comparison at different x/L for both configurations at α=0° and β=-5°

4.2.4 *Instantaneous vorticity field*

Up to this point, the analysis of the flow characteristics for the different model configurations and for the different attitudes has been performed on the ensemble average velocity fields. This approach neglects the unsteadiness of the flow and the dynamic behavior of the counter rotating vortices smoothing the intensity of the vorticity and broadening the sizes. In many cases, when the flow/structure interaction is important, the instantaneous behavior of the vortices cannot be neglected. The comparison between the mean peak vorticity with the instantaneous velocity fields shows a remarkably underestimation of the maximum peaks that in some cases can reach the 100%. The highly fragmented behavior of the instantaneous vorticity in part is due to the physics of the flow but in part is due to the presence of out layers.

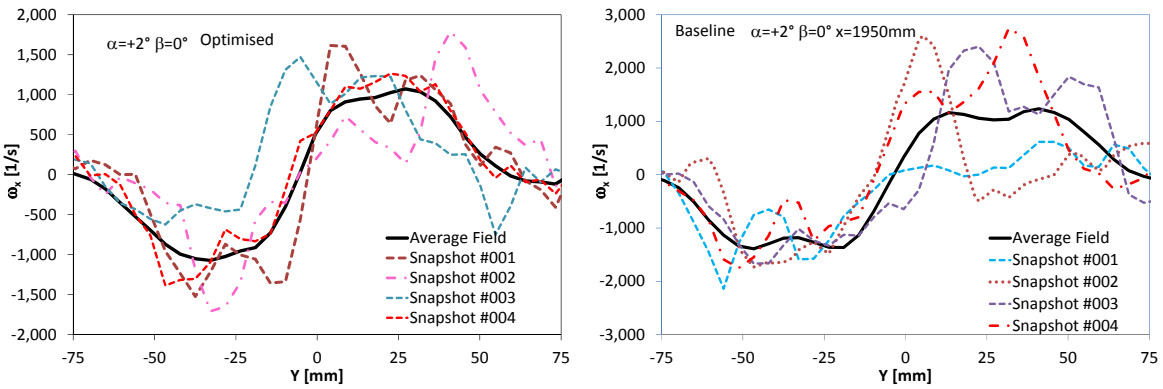

Figure 17: Instantaneous vs mean Vorticity peak comparison. Optimised (left) and Baseline (right).

The analysis of the out-of-plane vorticity colour map of a single snapshot can provide a better understanding. The instantaneous flow velocity is affected by several spurious vectors resulting in several peak of vorticity not related to the physics of the phenomena (Figure 18 left). On the other hand, the ensemble average velocity field broadens the size of the vortices and smooths the intensity of the vorticity (Figure 18 right). For the case presented the double negative and positive peaks presents on the instantaneous velocity map disappears in the ensemble velocity field. In order to remove the outliers the instantaneous velocity fields have been reconstructed using respectively the first 15 modes, 20 modes and 40 modes. The percentage energy content related to the selected modes was about 29% for 15 modes, 33% for 20 modes and 49% for 40 modes. The POD reconstructed velocity field presents higher vorticity peaks respect the ensemble average results also using a low number of modes and at the same time the bias affecting the images is mostly removed (Figure **19**). Using an energy content of the kinetic turbulent lower than the 50% (40 modes) the flow structures of the original image are reconstructed, the double positive and negative peaks are detected and the vorticity intensity is almost the same.

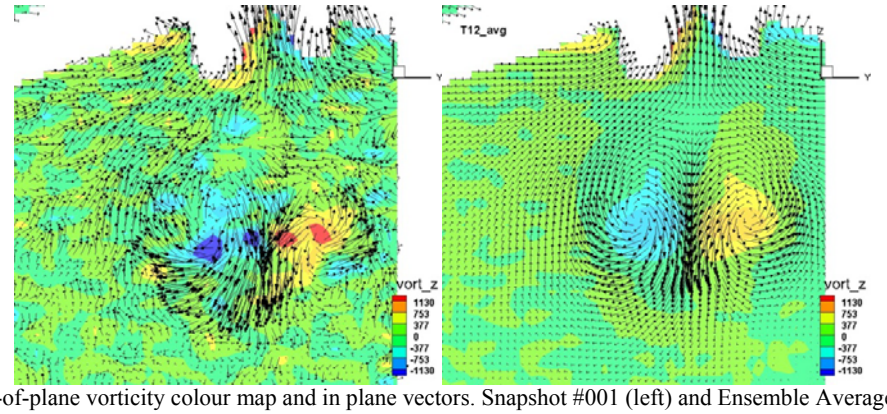

Figure 18: Out-of-plane vorticity colour map and in plane vectors. Snapshot #001 (left) and Ensemble Average (right) case at

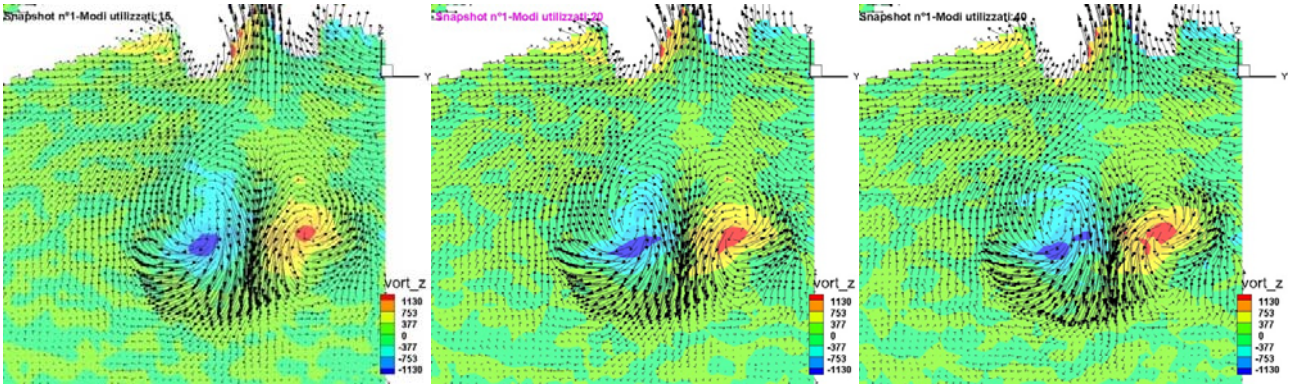

Figure 19: Snapshot #001 POD based low order reconstruction with 15 modes(left), 20 modes (centre) and 40 modes (right)

A quantitative comparison (Figure 20) presents for the first snapshot values of the maximum and minimum vorticity respectively larger than 50 and 40 percentage in comparison with the mean velocity field. The velocity field reconstructed with 15 modes recovers regarding the mean value about a 30% on the peak vorticity, the field reconstructed with 20 modes presents a positive peak larger than 40% and the negative peak larger than 31% in comparison with the mean velocity. The snapshot reconstructed with the first 40 modes recovers on the maximum and minimum peak of the mean velocity respectively the 43% and the 30%. Comparing with the original instantaneous vorticity field, a small underestimation of the vorticity peaks is still present but the vorticity distribution is more consistent with the fluid behavior. A summary of the discussed data for the first instantaneous velocity field is reported in Table 3. The use of POD for removing outliers from the instantaneous velocity fields, also on a limited number of samples, provides large benefits respect classical statistical methods and open the way to the automatic evaluation of the instantaneous vortex characteristics otherwise affected by large errors.

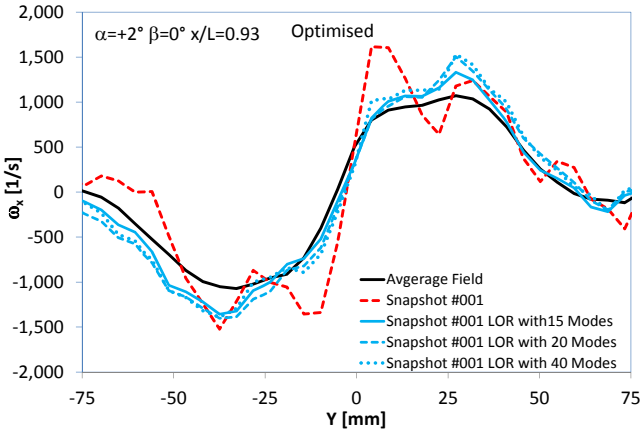

Figure 20: Mean, Instantaneous and POD reconstructed vorticity peaks comparison.

	Average	Snapshot #001	LOR with 15 modes	LOR with 20 modes	LOR with 40 modes
ω_{max}	1072	1615	1332	1504	1531
ω_{min}	-1072	-1524	-1357	-1403	-1390
$(\omega_{max}-\omega_{avg})/\omega_{avg}$	-	0.51	0.24	0.40	0.43
$(\omega_{min}-\omega_{avg})/\omega_{avg}$	-	0.42	0.27	0.31	0.30

Table 3: Summary of vorticity peak comparison between average, snapshot and low order reconstructed velocity.

5 CONCLUSIONS

A test campaign has been successfully performed at the RUAG LWTE wind tunnel with the goal to investigate the wake released by the baseline and optimised landing gear sponsons for the ERICA model. The optimised sponsons in comparison with the baseline configuration showed a drag reduction in the range between 15 to 30 drag counts and an efficiency increment for the model pitch angle varying between α=-5° to α=5° and null yaw angle β=0°. For β=-5°, the drag reduction of the optimized sponsons even increased varying from 21 to 37 drag counts. The S-PIV wake characterization has been performed at constant flow speed for different fuselage attitudes and yaw angles. The chosen S-PIV experimental set-up gave a high level of measurement productivity, resulting in a large amount of test conditions. \The measured velocity fields showed a pair of contra rotating vortices shedding downstream of the fuselage sponsons. The ensemble average results have been discussed in term of velocity magnitude, momentum, momentum loss and vorticity and related to the corresponding drag behavior. The instantaneous vorticity compared with the mean vorticity showed as the latter underestimated the real peak intensity. The POD-base low order reconstructed instantaneous velocity fields provides encouraging results for the outlier detection and removal without a detriment of the physical characteristics of the flow. From the PIV data the following conclusions can be drawn:

1. The flow field measurements indicate a clear wake reduction in terms of size and momentum loss. The percentage variation of the momentum loss presents a negative slop reaching the value of 3.7% and indicating the tendency to reach the values of the 2% correspondent to the drag reduction. Furthermore the vortex shedding for the optimised sponsons is delayed compared to the baseline, and the wake remains closer to the fuselage body.
2. The out of plane vorticity showed a notable intensity reduction by about 20% to 40% for the optimised sponsons in comparison to the baseline configuration. For β=-5° the optimised model presents a vorticity intensity reduction by about 20% to 50%, The wake evolution indicates a reduction of the left vortex intensity (negative peak) in opposition to the increment of the right vortex (positive peak). At x/L=0.93 the left vortex is almost vanished overwhelmed by the right vortex.
3. The instantaneous velocity field presented peak vorticity even higher than 100% with respect to the ensemble average velocity fields. This difference is in part due to the flow characteristics but in part to the outliers present in the velocity field. The POD-base low order reconstructed velocity fields removed the outliers with small detriment of the flow characteristics, the peak vorticity difference with the original snapshot was reduced to less than 10%.

ACKNOWLEDGMENT
The research activities presented throughout this paper have been partially funded by the European Community's Seventh Framework Program (FP/2007-2013) for the Clean Sky Joint Technology Initiative under grant agreement number: CSJU-GAM-GRC-2008-01. The authors would like to thank the Clean Sky Joint Undertaking for the financial and managing support. The authors would like to acknowledge the LWTE colleagues for the valuable support provided during the measurement campaign and dr. Davide Cinquegrana for the useful discussions about the use of POD.

REFERENCES

[1] Nannoni F, Giancamilli G and Cicalè M "ERICA: the european advanced tiltrotor" Proceeding of the 27th European Rotorcraft Forum (2001) pp. 55.1–55.15.
[2] Thomas ASW "Aircraft Drag Reduction Tecnology – A summary" AGARD R 723 (1985) pp 1.1 – 1.20.
[3] Campanardi G, Zanotti A and Macchi C "Final complete wind tunnel test database. technical report. Technical report" NICETRIP/POLIMI/WP4.TR007/4.0 (2008).
[4] Benini E and Ponza R "CODE-Tilt Proposal" JTI-CS-2010-1-GRC-02-004.
[5] Comis Da Ronco C, Ponza R and Benini E "Aerodynamic Shape Optimization in Aeronautics: A Fast and Effective Multi-Objective Approach" Archives of Computational Methods in Engineering Volume 21 Issue 3 (2014) pp 189-271.
[6] Ponza R "Assessment of tiltrotor fuselage drag reduction by wind tunnel tests and CFD (DREAm-TILT) Technical Proposal" GA no. 336439.
[7] De Gregorio F, Steiling D, Benini E, Ponza R "ERICA tiltrotor airframe wake characterization" Proceding of 41th European Rotorcraft Forum, Munich, Sept 1-3 (2015).
[8] Hackett JE, Sampath S and Phillips CG "Determination of wind tunnel constraint effects by a unified pressure signature method. Part 1: Applications to winged configurations" NASA-CR-166186 (1981).
[9] Anderson JD Jr "Fundamentals of aerodynamics" 2nd edition McGraw-Hill (1991).
[10] Hart DP "Super-Resolution PIV by Recursive Local-Correlation" Journal of Visualization Vol. 3 num: 2 (1999)
[11] Adrian RJ, "Particle Imaging Techniques for Experimental Fluid Mechanics" Annual Review of Fluid Mechanics, (1991) vol 23 pp 261-304.
[12] Raffel M, Willert C and Kompenhans J "Particle Image Velocimetry: A Practical Guide", Springer (2002)
[13] Brune GW "Quantitative Low-Speed Wake Surveys" Journal of Aircraft Volume 31 Number. 2 (1994) pp 249-255.
[14] Jones BM "The measurement of profile drag by the Pitot-Traverse method" ARC R&M 1688 (1936)
[15] Gunes H, Rist U "Spatial resolution enhancement/smoothing of stereo-particle-image-velocimetry data using proper-orthogonal-decomposition-based and kriging interpolation methods" Phys Fluids (2007) 19:064101–064119
[16] Wang HP, Gao Q, Feng LH, Wei RJ, Wang JJ "Proper orthogonal decomposition based outlier correction for PIV data" Exp Fluids (2015) 56:43
[17] Lumley JL (1967) The structure of inhomogeneous turbulent flows. In: Yaglom AM, Tatarski VI (eds) Atmospheric turbulence and radio wave propagation. Nauka, Moscow, pp 166–178
[18] Berkooz G, Holmes P, Lumley JL "The proper orthogonal decomposition in the analysis of turbulent flows" Ann Rev Fluid Mech 25 (1993) pp.539–575
[19] Sirovich L "Turbulence and the dynamics of coherent structures." Quart Appl Math 45 (1987) pp.561–590